Experimental reconstruction of primary hot isotopes and characteristic properties of the fragmenting source in heavy-ion reactions near the Fermi energy

W. Lin (林炜平),[1,2,*] X. Liu (刘星泉),[1,2] M. R. D. Rodrigues,[3] S. Kowalski,[4] R. Wada,[1,†] M. Huang (黄美容),[1] S. Zhang (张苏雅拉吐),[1,2] Z. Chen (陈志强),[1] J. Wang (王建松),[1] G. Q. Xiao (肖国青),[1] R. Han (韩瑞),[1] Z. Jin (靳增雪),[1,2] J. Liu (刘建立),[1] P. Ren (任培培),[1,2] F. Shi (石福栋),[1] T. Keutgen,[5] K. Hagel,[6] M. Barbui,[6] C. Bottosso,[6] A. Bonasera,[6,7] J. B. Natowitz,[6] T. Materna,[6] L. Qin (秦礼君),[6] P. K. Sahu,[6] and H. Zheng (郑华)[6,8]

[1]*Institute of Modern Physics, Chinese Academy of Sciences, Lanzhou 730000, China*

[2]*University of Chinese Academy of Sciences, Beijing 100049, China*

[3]*Instituto de Física, Universidade de São Paulo, Caixa Postal 66318, CEP 05389-970, São Paulo, SP, Brazil*

[4]*Institute of Physics, Silesia University, 40-007 Katowice, Poland*

[5]*FNRS and IPN, Université Catholique de Louvain, B-1348 Louvain-Neuve, Belgium*

[6]*Cyclotron Institute, Texas A&M University, College Station, Texas 77843, USA*

[7]*Laboratori Nazionali del Sud, INFN, via Santa Sofia, 62, 95123 Catania, Italy*

[8]*Physics Department, Texas A&M University, College Station, Texas 77843, USA*

(Received 25 April 2014; revised manuscript received 22 July 2014; published 6 October 2014)

The characteristic properties of the hot nuclear matter existing at the time of fragment formation in multifragmentation events produced in the reaction ^{64}Zn + ^{112}Sn at 40 MeV/nucleon are studied. A kinematical focusing method is employed to determine the multiplicities of evaporated light particles, associated with isotopically identified intermediate-mass fragments. From these data the primary isotopic yield distributions are reconstructed using a Monte Carlo method. The reconstructed yield distributions are in good agreement with the primary isotope distributions obtained from antisymmetrized molecular dynamics transport model simulations. Utilizing the reconstructed yields and power distribution, characteristic properties of the emitting source are examined. The primary mass distribution exhibits a power-law distribution with the critical exponent $A^{-2.3}$ for $A \geqslant 15$ isotopes but significantly deviate from that for lighter isotopes. Based on the modified Fisher model, the ratios of the Coulomb and symmetry energy coefficients relative to the temperature, a_c/T and $a_{\rm sym}/T$, are extracted as a function of A. The extracted $a_{\rm sym}/T$ values are compared with results of the antisymmetrized molecular dynamics simulations using Gogny interactions with different density dependencies of the symmetry energy term. The calculated $a_{\rm sym}/T$ values show a close relation to the symmetry energy at the density at the time of fragment formation. From this relation the density of the fragmenting source is determined to be $\rho/\rho_0 = 0.63 \pm 0.03$. Using this density, the symmetry energy coefficient and the temperature of fragmenting source are determined in a self-consistent manner as $a_{\rm sym} = 24.7 \pm 3.4$ MeV and $T = 4.9 \pm 0.2$ MeV.

DOI: 10.1103/PhysRevC.90.044603 PACS number(s): 25.70.Pq

I. INTRODUCTION

In violent heavy-ion collisions in the intermediate energy regime (20 MeV/nucleon $\leqslant E_{\rm inc} \leqslant$ a few hundred MeV/nucleon), intermediate-mass fragments (IMFs) are copiously produced in multifragmentation processes. Nuclear multifragmentation was predicted long ago [1] and has been extensively studied following the advent of 4π detectors [2–4]. Nuclear multifragmentation occurs when a large amount of energy is deposited in a finite nucleus. The multifragmentation process provides a wealth of information on nuclear dynamics, on the properties of the nuclear equation of state (EOS), and on possible nuclear phase transitions. The multifragmentation process was first suggested in the early 1980s [5–7] to provide possible evidence for a nuclear matter phase transition [3,8]. However, the specific properties of the nuclear phase transition in hot nuclear matter are still under debate.

The nuclear symmetry energy, a key part of the EOS, plays an important role in fragment generation in the multifragmentation process as well as in various phenomena in nuclear astrophysics, nuclear structure, and nuclear reactions. Determination of the density dependence of the symmetry energy has been a key objective in many recent laboratory experiments [9,10]. Investigations of the density dependence of the symmetry energy have been conducted using observables such as isotopic yield ratios [11], isospin diffusion [12], neutron-proton emission ratios [13], giant monopole resonances [14], pygmy dipole resonances [15], giant dipole resonances [16], collective flow [17], and isoscaling [18–20]. Different observables may probe the properties of the symmetry energy at different densities and temperatures.

In general, the nuclear multifragmentation process can be divided into three stages, i.e., dynamical compression and expansion, the formation of primary hot fragments, and, finally, the separation and cooling of the primary hot fragments by evaporation. To model the multifragmentation process, a number of models have been developed since the Boltzmann-Uehling-Uhlenbeck model [21], a test-particle-based Monte Carlo transport model, was coded in the 1980s. The stochastic

*linwp1204@impcas.ac.cn
†wada@comp.tamu.edu

mean field [22–24], Vlasov-Uehling-Uhlenbeck (VUU) [25], and Boltzmann-Nordheim-Vlasov [26] models are also based on the test-particle method. Instead of using test particles, Gaussian wave packets are introduced in quantum molecular dynamics such as the quantum molecular dynamics model [27–29]. The constrained molecular dynamics [30–33] and improved quantum molecular dynamics [34–38] models are based on quantum molecular dynamics, but an improved treatment is made in Pauli blocking during the time evolution of the reaction. The fermionic molecular dynamics [39] and antisymmetrized molecular dynamics (AMD) [40–42] models are the most sophisticated, in which the Pauli principle is taken into account in an exact manner in the time evolution of the wave packet and stochastic nucleon-nucleon collisions.

Most of these models can account reasonably well for many characteristic properties observed experimentally. On the other hand, statistical multifragmentation models such as the microcanonical metropolitan Monte Carlo model [43,44] and statistical multifragmentation model [44–52], based on a quite different assumption from the transport models, can also describe many experimental observables well. The statistical models use a freeze-out concept. Multifragmentation is assumed to take place in equilibrated nuclear matter described by parameters such as size, neutron/proton ratio, density, and temperature. In recent analyses the parameters are optimized to reproduce the experimental observables of the final state. In contrast, transport models do not assume any chemical or thermal equilibration. Nucleons travel in a mean field experiencing nucleon-nucleon collisions subject to the Pauli principle. The mean-field parameters and the in-medium nucleon-nucleon cross sections are the main physical ingredients. Fragmentation mechanisms also differ from those in statistical models.

One of the complications one has to face in comparing model predictions to experimental observables in either dynamical or statistical multifragmentation models is the secondary decay process. Multifragmentation is a very fast process, occurring in times of the order of 100 fm/c, whereas the secondary decay process is very slow. When fragments are formed in the multifragmentation process, many may be in excited states and will subsequently cool by secondary decay processes before they are detected [53–56]. The secondary cooling process may significantly alter the fragment yield distributions. Even though the statistical decay process itself is rather well understood and well coded, it is not a trivial task to combine it with a dynamical code. Statistical evaporation codes assume nuclei to be at thermal equilibrium with normal nuclear densities and shapes. These conditions are not guaranteed for fragments when they are formed in the multifragmentation process. We call the fragments at the time of formation "primary" fragments. Those observed after the cooling process are called the observed or "final" fragments [57–59].

In order to avoid the complications introduced by secondary decay and make the comparisons between experimental data and results from different models more straightforward, we proposed a kinematical reconstruction of the primary fragment yields. In previous work [55], we focused on the kinematical focusing method and the reconstruction of the excitation energy of primary fragments. In this article the characteristic properties of the fragmenting source are further investigated. A model study of the self-consistent method we have used in determination of the properties of the fragmenting source has been described in letter form in Ref. [56]. This article is organized as follows: The experimental procedure is described in Sec. II. Data analysis and reconstruction of the multiplicity of primary hot fragments are reported in Sec. III. Utilizing the reconstructed isotope yields, the power-low distribution is discussed in Sec. IV. Characteristic properties of the fragmenting system are studied in Sec. V. A brief summary is given in Sec. VI.

II. EXPERIMENT

The experiment was performed at the K-500 superconducting cyclotron facility at Texas A&M University. ^{64,70}Zn and ^{64}Ni beams were used to irradiate ^{58,64}Ni, ^{112,124}Sn, ^{197}Au, and ^{232}Th targets at 40 MeV/nucleon. In this article, we focus on the ^{64}Zn + ^{112}Sn reaction, which had the best statistical precision. Details of the experiment have been given in Refs. [55,58,62]. Here we briefly outline the experiment and clarify some issues. IMFs ($3 \leqslant Z \leqslant 18$) were detected by a detector telescope placed at $\theta_{\rm lab} = 20^\circ$. The telescope consisted of four Si detectors. Each Si detector had an effective area of 5×5 cm^2. The nominal detector thicknesses were 129, 300, 1000, and 1000 μm. All Si detectors were segmented into four sections and each quadrant subtended 5° in the polar angle. Typically six to eight isotopes for $3 \leqslant Z \leqslant 18$ were clearly identified using the $\Delta E \times E$ technique employing any two consecutive detectors. Mass identification of the isotopes was verified using a range-energy table [60]. The laboratory energy thresholds ranged from 4 to 10 MeV/nucleon, from Li isotopes to the heaviest isotopes identified.

Two sets of detectors were used to detect the light particles (LPs). For light-charged particles, 16 single-crystal CsI (Tl) detectors of 3-cm length were set around the target at angles between $\theta_{\rm Lab} = 27^\circ$ and $\theta_{\rm Lab} = 155^\circ$, tilted 30° in the azimuthal angle to avoid shadowing the neutron detectors described below. The light output from each detector was read by a photomultiplier tube. The pulse shape discrimination method was used to identify p, d, t, ^{3}He, and α particles. Energy calibrations for these particles were performed using Si detectors of 50 to 300 μm in front of the CsI detectors in a separate run.

For neutrons 16 detectors of the Belgian-French neutron detector array, DEMON, were used [61]. The setup of the neutron detectors is described in detail in Ref. [62]. Eight of them were set in the plane perpendicular to the reaction plane. The 0° in the polar and azimuthal angles of the opening angle was taken to be the telescope direction. The reaction plane of the neutron distribution from the observed IMF is defined by the vector of the telescope direction and that of the beam.

The other eight neutron detectors were set in the reaction plane. The detectors were distributed to achieve opening angles between the telescope and the DEMON detector of $15^\circ \leqslant \theta_{\text{IMF-}n} \leqslant 160^\circ$. Neutron/$\gamma$ discrimination was obtained from a pulse shape analysis, by comparing the slow component of the light output to the total light output. The neutron detection efficiency of the DEMON detector, averaged over the whole volume, was calculated using GEANT and applied to

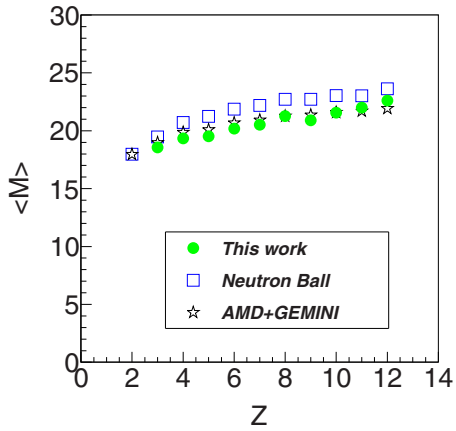

FIG. 1. (Color online) Comparisons of total neutron multiplicity obtained in this work (circles), from neutron ball measurement (squares), and from an AMD + GEMINI calculation (stars). The figure is taken from Ref. [55].

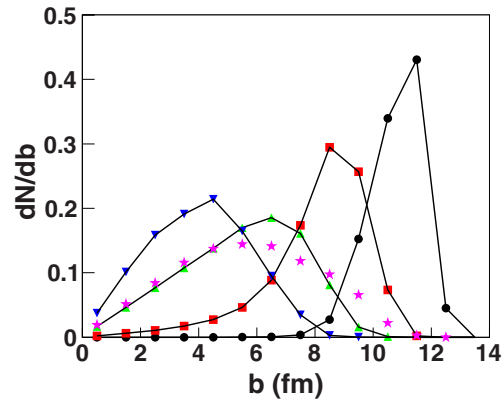

FIG. 2. (Color online) Simulated impact parameter distributions for violent (downward triangles), semiviolent (upward triangles), semiperipheral (squares), and peripheral (circles) collisions. Stars indicate events in which at least one IMF ($Z \geqslant 3$) is emitted at $20^\circ \pm 5^\circ$. The summed distribution for a given class is normalized to 1. The figure is taken from Ref. [58].

determine neutron multiplicities [62]. The derived multiplicities from this experiment are shown in Fig. 1, taken from Ref. [55]. In that figure they are also compared to results obtained in a separate experiment for the same reaction using the neutron ball calorimeter in the NIMROD detector array and to results of an AMD + GEMINI simulation of this reaction [41,63].

In the experiment, the telescope at $\theta_{\text{lab}} = 20^\circ$ was used as the main trigger. The angle of the telescope was optimized to be small enough so that sufficient IMF yields are obtained above the detector energy threshold but large enough so that the contribution from peripheral collisions was negligible according to AMD + GEMINI simulations. The events triggered by IMFs in this experiment are "inclusive," but they belong to a certain class of events. In order to determine the event class taken in this experiment, AMD simulations are used to evaluate the impact parameter range sampled and the IMF production mechanism involved in the present data set. In Fig. 2, calculated impact parameter distributions are presented. The violence of the reaction for each event in the AMD simulation is determined in the same way as in our previous work [64], in which the multiplicity of LPs, including neutrons, and the transverse energy of light charged particles were used.

The resultant impact parameter distributions are shown for each class of events together with those of events in which at least one IMF is emitted at an angle of $20^\circ \pm 5^\circ$. As shown in Fig. 2 the distribution of the events selected by the IMF detection is very similar to that of semiviolent collisions, which have a broad impact parameter distribution overlapping significantly with that of violent collisions.

The event class identification in this experiment is crucial for the following analysis. As shown in Ref. [64], IMFs from semiviolent collisions are dominant in the intermediate-velocity (IV) component in the moving-source analysis discussed below. Therefore in the following analysis it is assumed that the majority of the events triggered by IMFs at 20° in this experiment are representative of the IV-source component in semiviolent collisions.

Based on the assumption above, a moving-source fit was employed to fit the observed spectra [65]. For LPs, three sources—projectile-like (PLF), intermediate-velocity (IV), and target-like (TLF) sources—were assumed. For IMFs, a single IV source was used to extract the multiplicity. In Fig. 3, the experimental energy spectra of ^{16}O are compared with the results from an AMD + GEMINI calculation on an

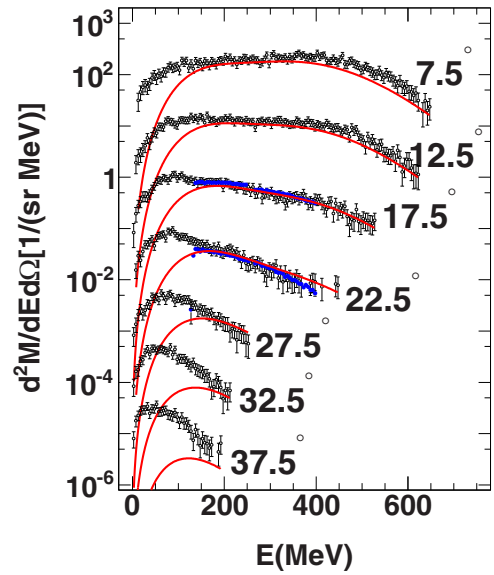

FIG. 3. (Color online) Experimental ^{16}O energy spectra (filled circles) are compared with the AMD + GEMINI result (open circles) for ^{64}Zn + ^{112}Sn at 40 MeV/nucleon. The spectrum for the AMD + GEMINI result was obtained for semiviolent collisions. Detection angles are given, the absolute Y scale corresponds to the bottom spectrum, and spectra are multiplied by a factor of 10 from bottom to the top. Curves are the result of a moving-source fit, in which the parameters were determined from the experimental spectra at 17.5° and 22.5°. Source velocities of $V_s = 0.62V_p$ and $\Delta V_s = 0.11V_p$ are used. The figure is taken from Ref. [58].

absolute scale, together with the moving-source fit result. Spectra for the AMD + GEMINI result are those corresponding to semiviolent collisions. The experimental spectra at 17.5° and 22.5° are reproduced reasonably by the AMD + GEMINI simulation. The moving-source parameters were determined from the experimental spectra. For IMFs, a fixed apparent temperature of 17 MeV was used. The IV source velocity was smeared between $V_s \pm \Delta V_s$. Typically $V_s = 0.6V_p$ and $\Delta V_s = 0.1V_p$ were used, where V_p is the projectile velocity, but for each case these values were optimized. The majority of the spectra at angles $\theta \leqslant 20°$ are well reproduced by the IV-source component, except for the lower energy side of these spectra and those at $\theta \geqslant 25°$. These are attributed to the TLF component. One can also see a small enhancement in the AMD + GEMINI result above the moving-source fit at forward angles, which is attributed to the PLF-source component. For semiperipheral or peripheral collisions, a prominent PLF component with a source velocity $Vs \sim 0.9V_p$ appears at forward angles. These are generally observed for all isotopes measured in the reaction presented here. In the following analysis, only the IV-source component is taken into account.

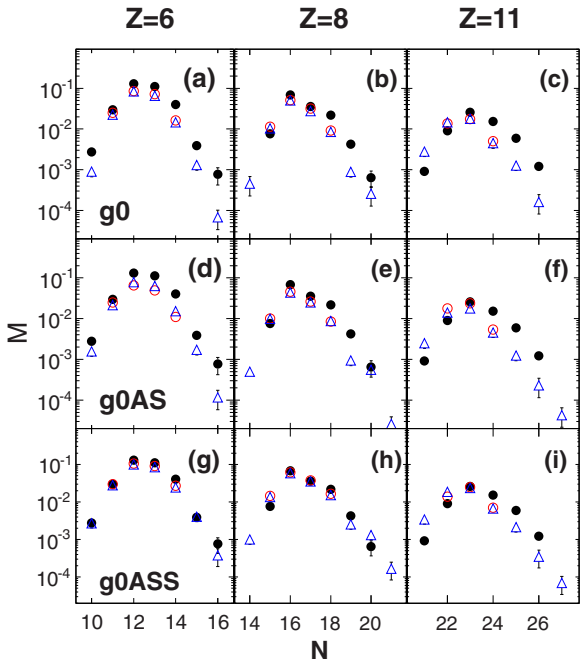

FIG. 4. (Color online) Typical cold-isotope distributions are compared with the results of AMD + GEMINI simulations for three interactions discussed in the paper. Results for $Z = 6$ (left column), 8 (middle column), and 11 (right column). Results of AMD with g0 (top row), g0AS (middle row), and g0ASS (bottom row) are plotted with the experimental data. Experimental data are taken from the IV source component from the moving-source fit and represented by filled circles. The same experimental data are used in each column. Multiplicity distributions from AMD simulations are calculated in two ways. Circles represent the results of the IV source component from the moving-source fit. Triangles are those calculated from the approximated method (see details in text).

In Fig. 4, the typical experimental cold-isotope distributions are compared with those of the AMD simulations. The experimental data are the IV-source component from the moving-source fit, described above. For AMD simulations, the IV multiplicities are calculated in two ways, one from the moving-source fit and the other by an approximated method. The approximated method is used because of the poor statistics in the yields of neutron-rich or proton-rich isotopes. As shown by the moving-source fit in Fig. 3, the IV-source component dominates in the energy range $E/A > 5$ MeV/nucleon and in the angular range $\theta < 25°$. The TLF component dominates in the energy range $E/A \leqslant 5$ MeV/nucleon over the entire angular range shown in the figure. The PLF component is barely seen in the high-energy range at $\theta = 5°$. The PLF contribution becomes significant at $\theta < 5°$ for isotopes with $A > 25$. Therefore in the approximated method the IV component is calculated by integrating yields at $E/A > 5$ MeV/nucleon and $5° < \theta < 25°$. The same energy and angular ranges are used for all isotopes. The calculated IV multiplicities in this method are compared with those of the moving-source fit in Fig. 4 for all AMD simulations. Good agreements are obtained for all cases in which the moving-source results are available.

III. RECONSTRUCTION OF THE PRIMARY HOT ISOTOPES

Yields of primary hot isotopes have been reconstructed, employing a kinematical focusing technique. In Fermi-energy heavy-ion collisions, LPs are emitted at different stages of the reaction and from different sources during the evolution of the collisions. Those from an excited isotope are kinematically focused into a cone centered along the isotope direction. The kinematical focusing technique uses this nature. The particles emitted from the precursor fragment of a detected isotope are called "correlated" particles and those not emitted from the precursor fragment are designated "uncorrelated" particles. To reconstruct the yield distributions of the primary hot isotopes, it is crucial to distinguish the correlated particles from the uncorrelated particles. When particles are emitted from a moving parent of an isotope (whose velocity is approximated by the velocity of the trigger IMF, $v_{\rm IMF}$), the isotropically emitted particles tend to be kinematically focused into a cone centered along the $v_{\rm IMF}$ vector. In the actual analysis, moving-source fits are employed to isolate the correlated LPs, including neutrons, from the uncorrelated ones and the correlated LP multiplicities are extracted for each isotope identified in the telescope.

The shape of the uncorrelated spectrum is obtained from the particle velocity spectrum observed in coincidence with Li isotopes, which is the minimum Z of the particle identified in the triggering telescope and associated with the fewest particle emissions [53,54]. Since the Li associated spectrum includes some precursor decay, the multiplicity extracted for a given isotope needs to be corrected by the addition of an amount corresponding to the correlated particle emission from the Li isotopes. This correction has been made using results from the AMD + GEMINI simulation. The amount of the correction was determined by averaging over values obtained

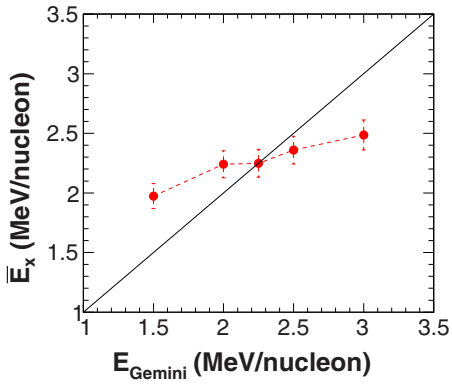

FIG. 5. (Color online) Average reconstructed excitation energy vs GEMINI input excitation energy.

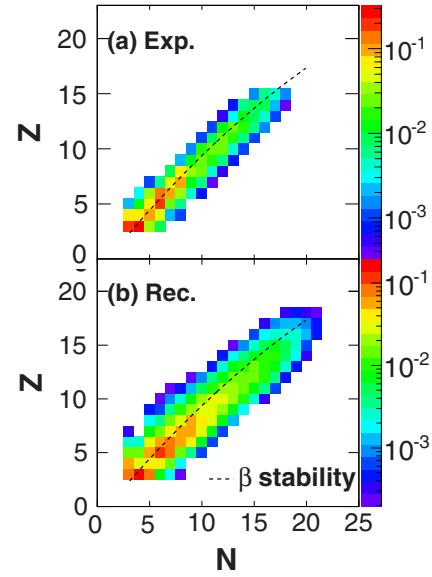

FIG. 6. (Color online) Isotope distribution in a two-dimensional plot of Z vs N (a) for experimental and (b) for reconstructed fragments. The dashed line is the β stability line. The Z axis is the multiplicity given on an absolute logarithmic scale.

in calculations using different EOSs (Gogny interaction of hard and soft EOSs) and different versions of the code (AMD/D [41] and AMD/DS [42]). Most of the extracted values agreed with each other within a rather small margin. These values are 0.40 ± 0.05 for neutrons, 0.24 ± 0.04 for protons, 0.044 ± 0.005 for deuterons, 0.035 ± 0.005 for tritons, and 0.32 ± 0.04 for α particles. The errors are evaluated from the standard deviations for the different calculations. The multiplicity of ^{3}He was not extracted in this experiment, because of the poor statistics, reflecting multiplicities much lower than those of deuterons and tritons. Therefore ^{3}He was not taken into account in the reconstruction analysis. A further detailed description of the kinematical focusing analysis is given in Ref. [55].

The excitation energies and multiplicity distributions of the primary hot isotopes were reconstructed using a Monte Carlo method, assuming that the LP emissions from an excited isotope are independent each other. Since only the average values of LP multiplicities can be extracted from this experiment, the shape (centroid and width) of the multiplicity distributions, assuming Gaussian distributions, have been taken from results of the statistical decay code, GEMINI [63]. The shape depends on the input excitation energy values of the GEMINI calculation. Several input values were used to reconstruct the excitation energy [55]. In Fig. 5 the average excitation energy per nucleon was calculated for isotopes with $Z \geqslant 6$, using their multiplicities as weighting factors. The resultant average excitation energies are compared with the input value of the GEMINI calculations and plotted. The input value and the extracted average energy coincide at $E_x \sim 2.25$ MeV/nucleon, and therefore in the following analysis, the input value of $E_x = 2.25 \pm 0.25$ MeV/nucleon was used for the GEMINI calculations to determine the shape of the multiplicity distribution.

The LP multiplicity distributions, M_i ($i = n,p,d,t,\alpha$), associated with a given detected daughter nucleus were generated on an event-by-event basis. For a given width of the Gaussian distribution, generated by the GEMINI simulation, their centroid is adjusted to give the same average multiplicity as that of the experiment. Using these LP multiplicities, the mass and charge of the primary hot isotopes with $A_{\rm hot}$ and $Z_{\rm hot}$ are calculated as

$$A_{\rm hot} = \sum_i M_i A_i + A_{\rm cold},$$
$$Z_{\rm hot} = \sum_i M_i Z_i + Z_{\rm cold}, \quad (1)$$

where A_i and Z_i are the mass and charge of correlated particle i, and $A_{\rm cold}$ and $Z_{\rm cold}$ are those of the detected cold isotope. One hundred thousand parents are generated for each experimentally observed isotope and added with the experimental multiplicity as a weighting factor. The multiplicities associated with the unstable nuclei of ^{8}Be and ^{9}B were added artificially by estimating their multiplicity and associated LP multiplicities from the neighboring isotopes. In Fig. 6, the isotopic distributions of the experimentally observed fragments and of the reconstructed hot fragments are shown in two-dimensional plots of Z vs N. The reconstructed primary distributions are significantly broader than those of the experimental cold fragments.

In Fig. 7 the multiplicity distributions of the reconstructed hot isotopes for each charge Z are shown together with the experimentally observed distributions. These are compared to the multiplicity distributions for the AMD primary fragments evaluated at $t = 300$ fm/c. At that time the clusters were identified using a standard coalescence technique with a coalescence radius in phase space of $R_c = 5$.

In order to determine the IV-source multiplicity for the AMD primary isotopes, the approximated method described in Sec. II. is employed, assuming that the energy and angular distributions of the primary isotopes are similar to those of the secondary cold isotopes. This assumptions are reasonable because the secondary emissions are isotropic in the GEMINI simulation.

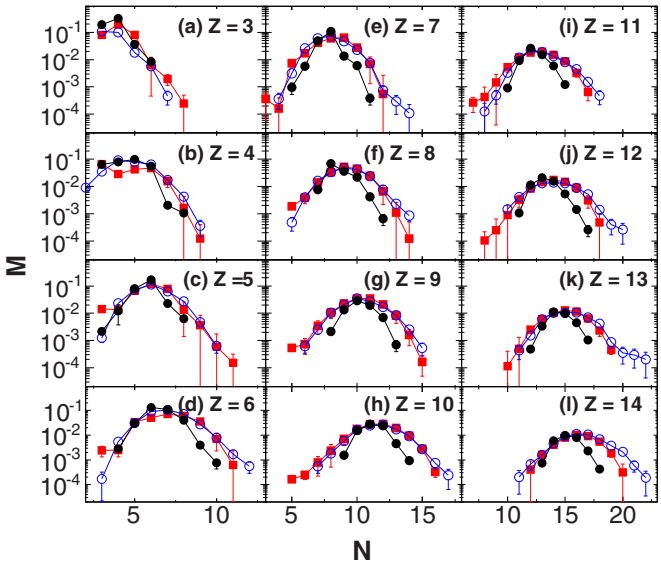

FIG. 7. (Color online) Isotopic multiplicity distributions of experimental cold fragments (filled circles), reconstructed hot fragments (filled squares), and AMD primary hot fragments as a function of fragment mass number A for a given charge Z, which is indicated. AMD results are from the g0AS interaction.

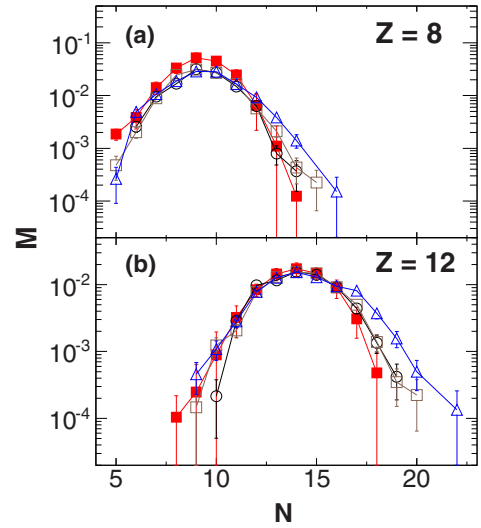

FIG. 8. (Color online) Isotopic multiplicity distributions of (a) $Z = 8$ and (b) $Z = 12$ for reconstructed hot fragments (filled squares) as well as AMD primary hot fragments with g0 (open circles), g0AS (open squares), and g0ASS (open triangles) as a function of the fragment mass number A for a given charge Z, which is indicated.

For the selection of semiviolent collisions, the events in the impact parameter range 0–8 fm are used. More than 75% of events in this range are semiviolent collisions as shown in Fig. 2.

In Fig. 7 comparisons of absolute multiplicity are shown. The reconstructed yields (filled squares) show distributions much wider than those of cold isotopes (dashed lines), which reflects the significant modification of the primary hot yield caused by the secondary decay process. The reconstructed yield distributions are compared with the yields of primary fragments from AMD simulations. Overall, the reconstructed primary isotope distributions are reasonably well reproduced by the AMD simulations. In Fig. 8 the reconstructed isotope distributions for $Z = 8$ and $Z = 12$ are further compared with primary distributions calculated with the standard Gogny interactions, i.e., g0, which has an asymptotic soft symmetry energy; g0AS, with an asymptotic stiff symmetry energy; and g0ASS, with an asymptotic superstiff symmetry energy [66].

The errors of the reconstructed multiplicities in Fig. 7 consist of errors in the associated LP multiplicities from the moving-source fit and errors in the amount added for the correction for emission from Li isotopes. Most of the combined errors are at most 10%–20%. For some very neutron- or proton-rich isotopes, a larger contribution of the additional error in the reconstructed isotope multiplicity is made by the choice of the input excitation energy for the shape of the LP multiplicity distribution calculation of GEMINI. For the errors shown in Fig. 7 the additional errors are evaluated from the maximum multiplicity difference in calculations with an excitation energy between 2.0 and 2.5 MeV/nucleon. In order to show the sensitivity of the selection of the GEMINI input excitation energy, all σ values are artificially changed between 0.75σ and 1.25σ, where σ is calculated for $E_x = 2.25$ MeV/nucleon. This is more or less the range of σ values when E_x is changed from 2.0 to 2.5 MeV/nucleon. The results are shown in Fig. 9. As one can see, only minor changes in the multiplicity distribution are observed. One should note that in actual simulations with different input excitation energies, the variation of σ is more or less random and therefore the observed effect is smaller.

As shown in Fig. 8, the reconstructed hot isotopic distributions are quite well reproduced by those of the AMD simulations with g0 and g0AS interactions, whereas those of the g0ASS show a slightly wider distribution. It is interesting to note that the g0ASS results show a better fit to the experimental secondary isotope distribution shown in Fig. 4. This better fit is "accidental" and caused by two factors: one is the higher excitation energy evaluation of the primary hot isotopes in AMD simulations, as discussed in Ref. [55]; and the other is the overprediction of the primary isotope distribution as shown

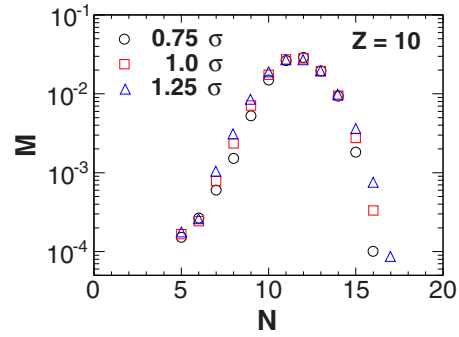

FIG. 9. (Color online) Calculated Ne isotope distributions when the σ values of the LP multiplicity distribution are changed from for 0.75σ to 1.25σ.

above. In AMD simulations, isotopes have an excitation energy in the range of 3–4 MeV/nucleon, whereas the evaluated experimental excitation energies are about 1 MeV/nucleon lower, depending on the isotopes. The wider distribution and the higher excitation energy more or less cancel out the yields of the cold isotopes and result in better fits for the g0ASS interaction in the secondary cold fragments. This fact indicates that it is important to separate the primary and secondary processes experimentally in order to refine the model simulations.

IV. POWER-LAW DISTRIBUTION

The multiplicities of the reconstructed primary isotopes are plotted as a function of A (filled circles) in Fig. 10, together with those of the AMD primary isotopes obtained with the g0AS interaction (open circles). The multiplicities are given on an absolute scale. The AMD multiplicities are the IV-source component, calculated by minimizing the projectile-like and target-like components as mentioned earlier. The yields of isotopes with $A \geqslant 15$ are well fitted by a power-law distribution of $A^{-2.3}$ for both the reconstructed and the AMD results. The falloff at $A > 30$ in the reconstructed results is caused by the limitation of the available isotopes, which can be used for the reconstruction ($Z \leqslant 14$). The associated LP multiplicities for $Z > 14$ were not extracted in this work, because of their low yields. The deviation from $A^{-2.3}$ in the AMD results at $A > 30$ is partially caused by the selection of the IV source in the approximate method. In this method most of the IV isotopes with $A > 30$ are gradually excluded by the angle selection condition $\theta_{\rm lab} > 5^\circ$, because the heavier fragments are focused at forward angles as A becomes larger. For isotopes with $A > 30$, it is very difficult to isolate the IV component from the PLF one in the approximate method. In order to show the effect of the angular condition, the yields of the IV + PLF components ($\theta < 25^\circ$) are plotted by filled triangles for $A > 30$. The yields show a power-law distribution with $A^{-2.3}$ roughly up to $A \sim 55$, with a slight overestimation from the PLF contribution.

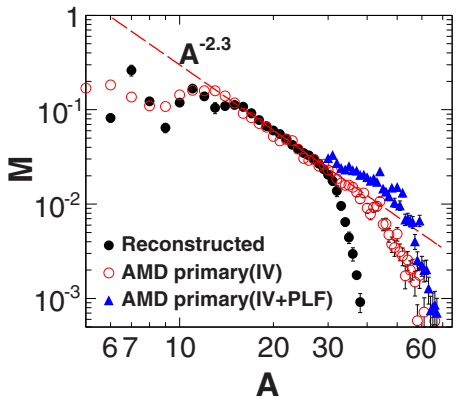

FIG. 10. (Color online) Absolute multiplicities of reconstructed hot isotopes are plotted by filled circles as a function of A together with those of the AMD primary isotopes of the IV source (open circles). Those of the IV + PLF sources (filled triangles) are plotted only for $A > 30$, where one can see a clear deviation from those of the IV source.

The power-law result is consistent with the previous power-law prediction in Ref. [58], though in that work the power law of $A^{-2.3}$ is predicted for all isotopes with $A \geqslant 1$. A significant deviation from the power-law distribution of $A^{-2.3}$ is observed for isotopes with $A < 15$ in Fig. 10 for both the reconstructed hot and the AMD primary isotopes. The reason for the flattering of the mass distribution below $A = 15$ is not clear at this moment. The power-law distribution observed in the AMD simulations should also be interpreted cautiously. Furuta *et al.* demonstrated in Ref. [67] that in AMD calculations, IMFs are formed over a wide range of time intervals (100–300 fm/c) and the isotope yield distribution changes with time. However, the yield and excitation energy distributions as a function of the mass at a given time can be identified as one of the statistically equilibrated ensembles generated by AMD separately. The temperature and density of the corresponding ensembles decrease monotonically in time. In Ref. [66], Ono *et al.* reported that isoscaling holds in AMD events, which is not evident *a priori* for dynamical models. Their study, therefore, may indicate that the variety of the fragmentation processes in AMD originates from the fluctuation of the statistical ensemble (a freeze-out ensemble) in time, density, and temperature. This large fluctuation may cause difficulty in identifying a single freeze-out source and time on an event-by-event basis. The existence of such a freeze-out source is assumed in all statistical multifragmentation models and they can reproduce the experimental observables reasonably well, as mentioned earlier. This fact and the observations in Refs. [66] and [67] suggest that the multifragmentation in AMD simulations reflects a large fluctuation of the virtual "freeze-out" in space, density, and time and causes a variety of cluster generations at early stages in the reaction. The experimental observation of the power-law distribution for $A \geqslant 15$ may suggest that there ia a virtual freeze-out volume for the production of heavier fragments, but for the production of lighter fragments dynamical processes, such as semitransparency [64,68] and neck emissions, become more important.

V. CHARACTERISTIC PROPERTIES OF THE FRAGMENTING SOURCE

The characteristic properties of the fragmenting source have been studied through the production of IMFs, using the modified Fisher model (MFM) [6,7,70,71]. The MFM is applied to characterize the emitting source of IMFs in previous work [56–58,69,70,72]. In the framework of the MFM, the yield of an isotope with $I = N - Z$ and A (N neutrons and Z protons) produced in a multifragmentation reaction can be given as

$$Y(I,A) = Y_0 \cdot A^{-\tau} \times \exp\left[\frac{W(I,A) + \mu_n N + \mu_p Z}{T} + S_{\rm mix}(I,A)\right]. \quad (2)$$

Using the generalized Weizsäcker-Bethe semiclassical mass formula [73,74], $W(I,A)$ can be approximated as

$$W(I,A) = a_v A - a_s A^{2/3} - a_c \frac{Z(Z-1)}{A^{1/3}} - a_{\rm sym}\frac{I^2}{A} - a_p \frac{\delta}{A^{1/2}}, \quad (3)$$

$$\delta = -\frac{(-1)^Z + (-1)^N}{2}.$$

In Eq. (2), $A^{-\tau}$ and $S_{\rm mix}(I,A) = N\ln(N/A) + Z\ln(Z/A)$ originate from the increases in the entropy and the mixing entropy at the time of fragment formation, respectively. μ_n (μ_p) is the neutron (proton) chemical potential. τ is the critical exponent. In this work, the value of $\tau = 2.3$ is adopted from previous studies [70]. In general, the coefficients, a_v, a_s, $a_{\rm sym}$, and a_p and the chemical potentials are temperature and density dependent, even though these dependences are not shown explicitly.

When one makes a yield ratio between isobars from Eq. (2), A-dependent parts are canceled out. Especially when isobars differing by 2 units in I are used, one can get the equation

$$\begin{aligned} R(I+2,I,A) &= Y(I+2,A)/Y(I,A) \\ &= \exp\{[\mu_n - \mu_p + 2a_c(Z-1)/A^{1/3} \\ &\quad - 4a_{\rm sym}(I+1)/A - \delta(N+1,Z-1) \\ &\quad - \delta(N,Z)]/T + \Delta(I+2,I,A)\}, \end{aligned} \quad (4)$$

where $\Delta(I+2,I,A) = S_{\rm mix}(I+2,A) - S_{\rm mix}(I,A)$. When the above equation is applied to the isobars with $I = N - Z = -1$ and 1, then the symmetry energy term and pairing term drop out and the following equation is obtained:

$$\ln[R(1,-1,A)] = [\Delta\mu + 2a_c(Z-1)/A^{1/3}]/T, \quad (5)$$

where $\Delta\mu = (\mu_n - \mu_p)$.

The $\ln R(1,-1,A)$ values in Eq. (5) are shown as a function of A in Fig. 11 for the experimental cold isotopes, those from the reconstructed hot ones extracted in the previous section and those from the AMD primary ones. Following the procedure described in Ref. [57], $a_c/T = 0.35$ from the experimental cold isotopes and $a_c/T = 0.18$ from the primary fragments of the AMD simulation with g0AS were obtained, and the fit curves are shown in Fig. 11 by solid and dashed lines, respectively. For reconstructed hot isotopes, using a_c/T and $\Delta\mu/T$ as free parameters, $a_c/T = 0.14 \pm 0.04$ and $\Delta\mu/T = 0.67$ are obtained and shown by the dotted line. The results from the reconstructed data show a significant difference from those from the experimental cold multiplicities and are distributed close to those of the AMD primary multiplicities, which is an indication of the sequential decay effect on the Coulomb parameter in Eq. (5).

In order to further study the characteristic properties of the source of the primary isotopes, the ratio of the symmetry energy coefficient relative to the temperature, $a_{\rm sym}/T$, is examined. In a similar way to that of Eq. (5), the $a_{\rm sym}/T$ value can be extracted using the yield ratio of three isobars, with $I = -1$, 1, and 3, as

$$\begin{aligned} a_{\rm sym}/T = -\frac{A}{8}\{&\ln[R(3,1,A)] - \ln[R(1,-1,A)] \\ &- \Delta(3,1,A) + \Delta E_c\}. \end{aligned} \quad (6)$$

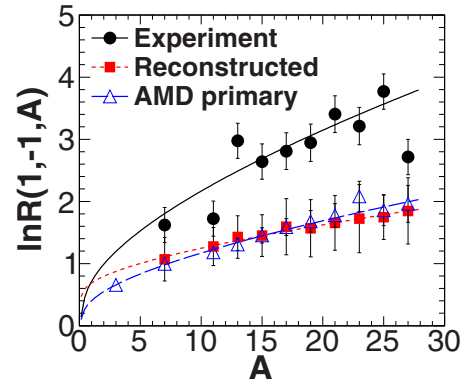

FIG. 11. (Color online) $\ln[R(1,-1,A)]$ values are plotted as a function of the fragment mass number A for experimental (filled circles) and reconstructed (filled squares) hot fragments as well as primary fragments of the AMD simulation (open triangles). Curves were obtained by free parameter search of $\Delta\mu/T$ and a_c/T in Eq. (5). The extracted parameter from the reconstructed data is $a_c/T = 0.14 \pm 0.04$, using $\Delta\mu/T = 0.67$. Values used for experimental and AMD primary data are from Ref. [57], and values of $(\Delta\mu/T, a_c/T) = (0.71, 0.35)$ for experimental and $(\Delta\mu/T, a_c/T) = (0.40, 0.18)$ for AMD primary data are used.

$\Delta(3,1,A)$ is the difference in mixing entropies of isobars A with $I = 3$ vs $I = 1$. ΔE_c is the difference in the Coulomb energy between neighboring isobars and is given by $\Delta E_c = 2a_c/(A^{1/3}T)$. The a_c value is obtained from the above analysis used in Fig. 11. One should note that the values of $\Delta(3,1,A)$ and ΔE_c are small compared to the first two terms and they have opposite signs to each other.

In a transport model such as AMD, the dynamic evolution of the system is such that variations in the temperature, density, and symmetry energy are closely correlated with each other. If one of these parameters is determined, then other parameters can be extracted in a self-consistent manner from the transport model solutions using these relationships. In the following the experimentally extracted $a_{\rm sym}/T$ values from the reconstructed isotopes are compared with those from the AMD simulations using g0, g0AS, and g0ASS interactions. From the comparisons, the density of the fragmenting source is determined and then the temperature and symmetry energy are extracted using the model-predicted correlations. This method has been applied in Refs. [56] and [72].

Using Eq. (6), $a_{\rm sym}/T$ values were calculated and the results are shown in Fig. 12. The results from the reconstructed primary isotopes (filled squares) show a rather flat distribution and a significant difference from those for the experimentally observed cold isotopes (filled circles), indicating that the strong mass dependence of the latter originates from the secondary cooling process as concluded in Ref. [57]. AMD results with the three interactions show a similar flat distribution to those of the reconstructed ones. Their distributions are more or less parallel to each other but have different values. Their average values are given in the fifth column of Table I.

The ratios $a_{\rm sym}/T$ for g0 relative to those for g0AS and g0ASS are plotted in Fig. 13(a), together with the ratio of those from g0 relative to those from the reconstructed yields

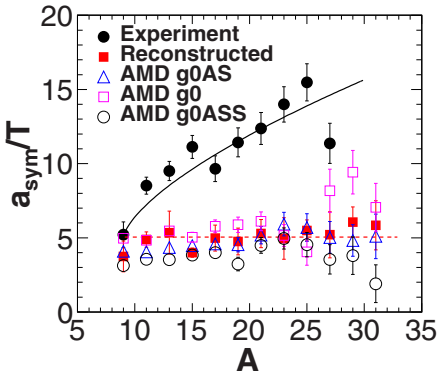

FIG. 12. (Color online) Calculated values of a_{sym}/T, are plotted as a function of A from experimental cold isotopes (filled circles) and reconstructed hot isotopes (filled squares). The solid curve is from Ref. [57]. The dashed curve is the average value of those from the reconstructed ones. AMD results are shown by open symbols: g0 (squares), g0AS (triangles), and g0ASS (circles). The average a_{sym}/T values for those from reconstructed and AMD simulations are listed in the fifth column in Table I.

(filled circles). Both of the calculated ratios are more or less constant as a function of A, though those from the reconstructed yields have a slightly larger fluctuation than those from simulations. The average values of these ratios are given in the second column in Table I. Following Ref. [66], we interpret the ratios as resulting from the difference in the symmetry energy coefficient at the density and temperature of fragment formation. In Fig. 13(b), the density dependence of the symmetry energy coefficient for g0, g0AS, and g0ASS is shown as a function of ρ/ρ_0. In Fig. 13(c), their ratios for g0/g0AS and g0/g0ASS are shown. From the ratio values of the simulations in Fig. 13(a), the corresponding densities are extracted as indicated by the vertical hatched areas in Figs. 13(b) and 13(c). The extracted values are $\rho/\rho_0 = 0.61 \pm 0.05$ for g0/g0AS and $\rho/\rho_0 = 0.63 \pm 0.03$ for g0/g0ASS. These are given in the third column in Table I. The error becomes smaller for g0/g0ASS because the ratio of g0/g0ASS shows a sharper slope as a function of the density and therefore a greater sensitivity to the density dependence. Assuming that the nucleon density is same for the three

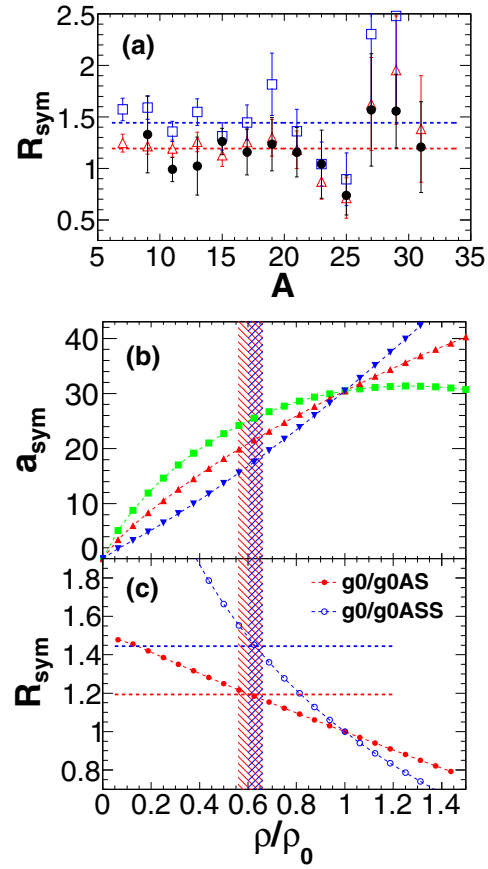

FIG. 13. (Color online) (a) Ratios of the calculated a_{sym}/T values for g0/g0AS (open triangles), g0/g0ASS (open squares), and g0/reconstructed experimental yield (filled circles). Dotted lines are the average values for AMD simulations. The values are listed in the second column in Table I. (b) Symmetry energy coefficient vs density for g0, g0AS, and g0ASS used in AMD simulations. The hatched vertical area indicates the density of the fragmenting system extracted from the ratio of the symmetry energy coefficient. Two hatching patterns are used for the density values given in the third column in Table I. (c) Ratio of symmetry energy coefficients used in (b), g0/g0AS and g0/g0ASS, as a function of the density. Dotted horizontal lines indicate ratio values extracted from the a_{sym}/T values in (a).

TABLE I. Extracted parameters. E_x values (in MeV; bottom three rows) are from Ref. [75].

	Ratio	ρ/ρ_0	a_{sym} (MeV)	a_{sym}/T	T (MeV)
g0			$25. \pm 0.6$	5.29 ± 0.13	4.9 ± 0.2
g0/g0AS	1.19 ± 0.03	0.61 ± 0.05			
g0AS			21.2 ± 1.2	4.31 ± 0.12	4.9 ± 0.4
g0/g0ASS	1.44 ± 0.05	0.63 ± 0.03			
g0ASS			17.8 ± 0.9	3.50 ± 0.12	5.1 ± 0.5
Expt.		0.63 ± 0.03	24.7 ± 1.9	5.04 ± 0.32	4.9 ± 0.2
E_x (MeV)					
5		0.50 ± 0.12	20 ± 2		5.7 ± 0.5
7.5		0.45 ± 0.12	17 ± 2		6.5 ± 0.5
9.5		0.30 ± 0.12	16 ± 2		7.0 ± 0.5

interactions used, the nucleon density of the fragmenting system is determined from the overlap value of the extracted values as $\rho/\rho_0 = 0.63 \pm 0.03$. This assumption is reasonable because the nucleon density is mainly determined by the stiffness of the EOS and not by the density dependence of the symmetry energy term.

The corresponding symmetry energy coefficient values from the calculations are extracted from Fig. 13(b) as 25.7 ± 0.6, 21.2 ± 1.2, and 17.8 ± 0.9 MeV for g0, g0AS, and g0ASS, respectively. These values are given in the fourth column in Table I. For AMD simulations, the temperature, $T = a_{\rm sym}/(a_{\rm sym}/T)$, is calculated. We find $T = 4.9 \pm 0.2, 4.9 \pm 0.4$, and 5.1 ± 0.5 MeV, respectively, for the g0, g0AS, and g0ASS interactions. The temperatures are listed in the final column in Table I. One should note that the errors for the temperature and symmetry energy values originate from those in the density values and the $a_{\rm sym}/T$ values in the second and fifth columns in Table I, since they are determined using their predicted correlations in the AMD model.

From the temperature values for the AMD simulations with different interactions, the temperature for the fragmenting source is determined from the overlap values, assuming the same source temperature for the different density dependencies of the symmetry energy coefficient. The overlap value is $T = 4.9 \pm 0.2$ MeV. Using this temperature and the experimental $a_{\rm sym}/T$ value at the bottom of the fifth column, the experimental symmetry energy coefficient is determined as $a_{\rm sym} = 24.7 \pm 1.9$ MeV. The extracted symmetry energy coefficient, temperature, and density for fragment formation show notable differences from those in Ref. [75], where the values were extracted from the experimentally observed secondary yields using isoscaling parameters. In that work, the reactions of ^{40}Ar, ^{40}Ca + ^{58}Ni, and ^{58}Fe at 25–55 MeV/nucleon were studied. Isoscaling parameters were extracted from the experiments and compared to those of the AMD and statistical multifragmentation model simulations using interactions with different density dependencies of the symmetry energy. From those comparisons, the values listed in the bottom three rows in Table I were obtained.

VI. SUMMARY

The multiplicity distribution of primary hot isotopes was experimentally reconstructed for fragments produced in the ^{64}Zn + ^{112}Sn reaction at 40 MeV/nucleon. A kinematical focusing technique was employed to isolate particles emitted from the primary fragments. Using the experimental multiplicities of isotopically identified detected fragments and their associated LP multiplicities together with LP distribution widths from a GEMINI simulation, a Monte Carlo method was used for the reconstruction. The multiplicity distributions of the reconstructed primary fragments are in good agreement with those calculated from the AMD with g0 or g0AS interactions. The results for g0ASS exhibit a slightly wider distribution in neutron number. The mass yields of the reconstructed hot isotopes for $A \geqslant 15$ show a power-law distribution of $A^{-2.3}$, whereas those with $A < 15$ show a significant deviation from that, suggesting that the production mechanism for these lighter isotopes are different from those for heavier ones. This power-law behavior together with other statistical natures may reflect the fact that there is a virtual "freeze-out" in transport models and a large fluctuation in space and time causes a variety of cluster generation at early stages of the reaction.

The ratios of the symmetry energy coefficients to the temperature, $a_{\rm sym}/T$, extracted based on the MFM, were utilized to determine the density, temperature, and symmetry energy coefficient at the time of fragment formation in a self-consistent way. From the comparisons with AMD simulations using different interactions, $\rho/\rho_0 = 0.63 \pm 0.03$, a temperature of $T = 4.9 \pm 0.2$ MeV and a symmetry energy coefficient of $a_{\rm sym} = 24.7 \pm 1.9$ MeV are extracted at the time of the reconstructed primary isotope formation.

ACKNOWLEDGMENTS

We thank the staff of the Texas A&M Cyclotron facility for their support during the experiment. We thank the Institute of Nuclear Physics of the University of Louvain and Prof. Y. El Masri for allowing us to use the DEMON detectors. We also thank A. Ono and R. J. Charity for providing their codes. This work was supported by the US Department of Energy under Grant No. DE-FG03-93ER40773 and the Robert A. Welch Foundation under Grant No. A0330. This work was also supported by the National Natural Science Foundation of China (Grant Nos. 11075189 and 11105187) and the 100 Persons Project (Grant Nos. 0910020BR0 and Y010110BR0) and ADS Project 302 of the Chinese Academy of Sciences (Grant No. XDA03030200). R.W. thanks the program of the Visiting Professorship of Senior International Scientists of the Chinese Academy of Science for their support.

[1] N. Bohr, Nature **137**, 344 (1936).
[2] B. Borderie and M. F. Rivet, Prog. Part. Nucl. Phys. **61**, 551 (2008).
[3] F. Gulminelli *et al.*, Eur. Phys. J. A **30**, 1 (2006), and related topics in the volume.
[4] Ph. Chomaz *et al.*, Phys. Rep. **389**, 263 (2004).
[5] J. E. Finn *et al.*, Phys. Rev. Lett. **49**, 1321 (1982).
[6] R. W. Minich *et al.*, Phys. Lett. B **118**, 458 (1982).
[7] A. S. Hirsch *et al.*, Nucl. Phys. A **418**, 267 (1984).
[8] J. B. Elliott *et al.*, Phys. Rev. C **62**, 064603 (2000); Phys. Rev. Lett. **88**, 042701 (2002); Phys. Rev. C **67**, 024609 (2003).
[9] J. M. Lattimer and M. Prakash, Science **304**, 536 (2004).
[10] B. A. Li *et al.* Phys. Rep. **464**, 113 (2008).
[11] M. B. Tsang, W. A. Friedman, C. K. Gelbke, W. G. Lynch, G. Verde, and H. S. Xu, Phys. Rev. Lett. **86**, 5023 (2001).
[12] M. B. Tsang *et al.*, Phys. Rev. Lett. **92**, 062701 (2004).
[13] M. A. Famiano *et al.*, Phys. Rev. Lett. **97**, 052701 (2006).
[14] T. Li *et al.*, Phys. Rev. Lett. **99**, 162503 (2007).
[15] A. Klimkiewicz *et al.*, Phys. Rev. C **76**, 051603 (2007).
[16] L. Trippa, G. Colò, and E. Vigezzi, Phys. Rev. C **77**, 061304 (2008).
[17] Z. Kohley *et al.*, Phys. Rev. C **85**, 064605 (2012).

[18] H. S. Xu *et al.*, Phys. Rev. Lett. **85**, 716 (2000).
[19] M. B. Tsang *et al.*, Phys. Rev. C **64**, 054615 (2001).
[20] M. Huang *et al.*, Nucl. Phys. A **847**, 233 (2010).
[21] J. Aichelin and G. Bertsch, Phys. Rev. C **31**, 1730 (1985).
[22] M. Colonna *et al.*, Nucl. Phys. A **642**, 449 (1998).
[23] V. Baran, M. Colonna, M. Di Toro, and R. Zus, Phys. Rev. C **85**, 054611 (2012).
[24] F. Gagnon-Moisan *et al.*, Phys. Rev. C **86**, 044617 (2012).
[25] H. Kruse, B. V. Jacak, J. J. Molitoris, G. D. Westfall, and H. Stöcker, Phys. Rev. C **31**, 1770 (1985).
[26] V. Baran *et al.*, Nucl. Phys. A **703**, 603 (2002).
[27] G. Peilert, H. Stöcker, W. Greiner, A. Rosenhauer, A. Bohnet, and J. Aichelin, Phys. Rev. C **39**, 1402 (1989).
[28] J. Aichelin, Phys. Rep. **202**, 233 (1991).
[29] J. Lukasik *et al.*, Acta Phys. Polon. **B24**, 1959 (1993).
[30] M. Papa, T. Maruyama, and A. Bonasera, Phys. Rev. C **64**, 024612 (2001).
[31] M. Papa, G. Giuliani, and A. Bonasera, J. Comput. Phys. **208**, 403 (2005).
[32] M. Papa *et al.*, Phys. Rev. C **75**, 054616 (2007).
[33] M. Papa and G. Giuliani, Eur. Phys. J. A **39**, 117 (2009).
[34] N. Wang, Z. Li, and X. Wu, Phys. Rev. C **65**, 064608 (2002).
[35] N. Wang, Z. Li, X. Wu, J. Tian, Y. Zhang, and M. Liu, Phys. Rev. C **69**, 034608 (2004).
[36] Y. Zhang and Z. Li, Phys. Rev. C **71**, 024604 (2005).
[37] Y. Zhang and Z. Li, Phys. Rev. C **74**, 014602 (2006).
[38] Y. Zhang *et al.*, Phys. Rev. C **85**, 024602 (2012).
[39] H. Feldmeier, Nucl. Phys. A **515**, 147 (1990).
[40] A. Ono and H. Horiuchi, Phys. Rev. C **53**, 2958 (1996).
[41] A. Ono, Phys. Rev. C **59**, 853 (1999).
[42] A. Ono, S. Hudan, A. Chbihi, and J. D. Frankland, Phys. Rev. C **66**, 014603 (2002).
[43] D. H. E. Gross, Rep. Prog. Phys. **53**, 605 (1990).
[44] M. D'Agostino *et al.*, Nucl. Phys. A **650**, 329 (1999).
[45] J. P. Bondorf, R. Donangelo, and I. N. Mishustin, Nucl. Phys. A **443**, 321 (1985).
[46] J. Bondorf, A. S. Botvina, A. S. Iljinov, I. N. Mishutin, and K. Sneppen, Phys. Rep. **257**, 133 (1995).
[47] A. S. Botvina *et al.*, Nucl. Phys. A **584**, 737 (1995).
[48] M. D'Agostino *et al.*, Phys. Lett. B **371**, 175 (1996).
[49] R. P. Scharenberg *et al.*, Phys. Rev. C **64**, 054602 (2001).
[50] N. Bellaize *et al.*, Nucl. Phys. A **709**, 367 (2002).
[51] S. P. Avdeyev *et al.*, Nucl. Phys. A **709**, 392 (2002).
[52] R. Ogul *et al.*, Phys. Rev. C **83**, 024608 (2011).
[53] N. Marie *et al.*, Phys. Rev. C **58**, 256 (1998).
[54] S. Hudan *et al.*, Phys. Rev. C **67**, 064613 (2003).
[55] M. R. D. Rodrigues *et al.*, Phys. Rev. C **88**, 034605 (2013).
[56] W. Lin *et al.*, Phys. Rev. C **89**, 021601(R) (2014).
[57] M. Huang *et al.*, Phys. Rev. C **81**, 044620 (2010).
[58] M. Huang *et al.*, Phys. Rev. C **82**, 054602 (2010).
[59] Z. Chen *et al.*, Phys. Rev. C **81**, 064613 (2010).
[60] F. Hubert, R. Bimbot, and H. Gauvin, At. Data Nucl. Data Tables **46**, 1 (1990).
[61] I. Tilquin *et al.*, Nucl. Instr. Meth. A **365**, 446 (1995).
[62] S. Zhang *et al.*, Nucl. Instr. Meth. A. **709**, 68 (2013).
[63] R. J. Charity *et al.*, Nucl. Phys. A **483**, 371 (1988).
[64] R. Wada *et al.*, Phys. Rev. C **69**, 044610 (2004).
[65] T. C. Awes, G. Poggi, C. K. Gelbke, B. B. Back, B. G. Glagola, H. Breuer, and V. E. Viola, Jr., Phys. Rev. C **24**, 89 (1981).
[66] A. Ono, P. Danielewicz, W. A. Friedman, W. G. Lynch, and M. B. Tsang, Phys. Rev. C **68**, 051601(R) (2003). For g0AS, $x = -1/2$ and, for g0ASS, $x = -2$ are used in Eq. (2) in this reference.
[67] T. Furuta and A. Ono, Phys. Rev. C **79**, 014608 (2009).
[68] R. Wada *et al.*, Phys. Rev. C **62**, 034601 (2000).
[69] M. Huang *et al.*, Phys. Rev. C **81**, 044618 (2010).
[70] A. Bonasera *et al.*, Phys. Rev. Lett. **101**, 122702 (2008).
[71] M. E. Fisher, Rep. Prog. Phys. **30**, 615 (1967).
[72] X. Liu *et al.*, Phys. Rev. C **90**, 014605 (2014).
[73] C. F. von Weizsäcker, Z. Phys. **96**, 431 (1935).
[74] H. A. Bethe, Rev. Mod. Phys. **8**, 82 (1936).
[75] D. V. Shetty, S. J. Yennello, and G. A. Souliotis, Phys. Rev. C **76**, 024606 (2007).